Fabrication, Design and Noise Analysis of a High-Gain Waveguide-Coupled Photoconductive Detector

Nicholas C. Harris

A thesis submitted in partial fulfillment of the requirements for the degree of

Master of Science in Electrical Engineering

University of Washington

2012

Committee

Michael Hochberg

Mani Soma

Program Authorized to Offer Degree:

Electrical Engineering

Abstract

Fabrication, Design and Noise Analysis of a High-Gain Waveguide-Coupled Photoconductive Detector

Nicholas C. Harris

Chair of Supervisory Committee:

Michael Hochberg

Assistant Professor of Electrical Engineering

In the field of silicon photonics, it has only recently become possible to build complex systems. As system power constraints and complexity increase, design margins will decrease—making understanding device noise performance and device-specific noise origins increasingly necessary. Approaches to increased photodetector responsivity are also of great importance, since they can significantly improve overall system performance. The design, theory, fabrication and testing of a waveguide-coupled germanium MSM photodetector with an above-unity quantum efficiency of approximately 140% is presented, capable of 1.1 GHz operation. The current amplification comes from the photoconductive multiplication effect. The noise elbow at 5V bias is measured to be approximately 150MHz and the high frequency detector noise approaches the Johnson noise floor. I demonstrate for the first time that Ge on Si based

photoconductors are not limited by shot noise, as conventional PIN detectors are, but in fact achieve lower noise figures of merit.

Dedication

To my family.

Table of Contents

Table of Figures

Chapter 1. Introduction

1.1 Integrated Photonics

It has been the trend for a number of years to simply increase the parallelism of CMOS electronic circuitry and metallic interconnects in order to achieve higher bandwidth—resulting in growing die area requirements and power consumption. Silicon photonics has recently emerged as the leading competitor in overcoming these issues. The integration that has occurred between waveguides and photodetectors has been critical in enabling this new technology. Perhaps surprisingly, silicon has been shown to be an excellent material system for the fabrication of high-speed photonic devices. The ubiquity of silicon in CMOS electronics manufacturing, as well as large investments in silicon-based foundries, has largely reduced the cost of development in this material system. It is plausible that this resulting economic advantage may be leveraged in silicon photonics. The ability to use standard CMOS processing techniques to produce high-speed photonic devices further adds to the synergy between CMOS and silicon photonics.

Long distance communication systems have played a key role in the Information Age. The transition from traditional metallic transmission to fiber-optics revolutionized the communications industry for several reasons. Signals propagating in metal suffer from severe attenuation and are subject to interference. These two issues result in the necessity for frequent usage of signal recovery and amplification hardware. The low loss and low interference susceptibility of photonic links makes this type of signal recovery hardware less necessary. Modulators and photodetectors are two critical components in a photonic link. Both of these components, traditionally built in III-V group material systems and packaged as discrete devices, are produced with high yield and in vast

numbers on a single silicon-photonic chip. Compared to integrated systems, current discrete component systems do not lend themselves to high complexity. Silicon photonics may have the opportunity to introduce new and exciting system possibilities to the long distance communications industry.

There are many opportunities on a smaller scale as well. Mainboards with chips separated by centimeters require many bus lines for communication. For some time, the trend for microprocessors has been increasing pin counts resulting in ever-increasing mainboard parallel metal traces to accommodate the required bandwidth. This issue creates an opportunity to serialize many of these metal traces into an optical fiber supported by a photonic IO interface. On an even smaller scale, utilizing photonics in multi-core applications for core-to-core communications provides an attractive means through which die area and supporting circuitry may be decreased. Perhaps one of the most exciting new areas of research capable of utilizing this technology is quantum optics. It has recently become possible to replace entire manually aligned optical bench setups with a single chip. Eliminating the tedium of bench-top setups both reduces the barrier to experimentation and eliminates the issue of optical alignment.

1.2 Germanium Photodetectors

Germanium has gained widespread preference as an optical detection medium due to its compatibility with the 1550 nm communications standard as well as for its amenability with CMOS front-end processing [1,2,3]. Although germanium waveguide-coupled detectors operating at 40Gbps and higher have been demonstrated using mainly standard CMOS processes, the noise characteristics of these devices has not been reported in detail [1,4,5,6,7,8,9]. Some basic noise measurements have recently been

done for PIN photodetectors [6,10]. The noise present in photodetectors will be a limitation for analog applications, and it will be a factor in determining the number of photons per bit required for digital applications—driving system power budgets. This will necessitate device and system level design techniques that counter reduced signal to noise ratios and enable devices with high sensitivity.

1.3 Photoconductive Detectors

Known as either "MSM photodetectors" or "photoconductive detectors", these devices consist of a slab of semiconductor with current-injecting contacts affixed at either end. It is generally assumed that all current passing through a photodetector, dark or illuminated, will contribute to noise. However, it will be demonstrated for the first time that Ge on Si based photoconductors are not limited by shot noise, as conventional PIN detectors are, but in fact achieve lower noise figures of merit.

For the photoconductive detector demonstrated here, only a fraction of the aggregate dark current contributes to shot noise produced by the device. In systems operated at low temperatures and frequencies above a few hundred MHz, shot noise becomes the largest contributor to the device noise—since thermal noise power is proportional to temperature. The ability to decrease the shot noise then directly benefits the signal to noise ratio (SNR) of the system. Low defect density epitaxial germanium, approaching intrinsic quality, may enable a path forward for decreasing device shot noise, yielding high impedance and lower dark current for Si-Ge photoconductive detectors. This fractional contribution to shot noise will prove to be an attractive feature in the selection of photoconductive detectors for complex, low-noise photonic systems.

Chapter 2. Photodetection

2.1 Operation

As a necessary component in optical links, photodetectors facilitate optical transduction. While various implementations of photodetector have been realized, attention will be given to photoconductive detectors. In intrinsic photoconductors, photoexcitation occurs between the valence and conduction band, while in extrinsic photoconductors, electron hole pair generation and excitation involves the induced impurity state transitions. This process is illustrated in fig. 1, below.

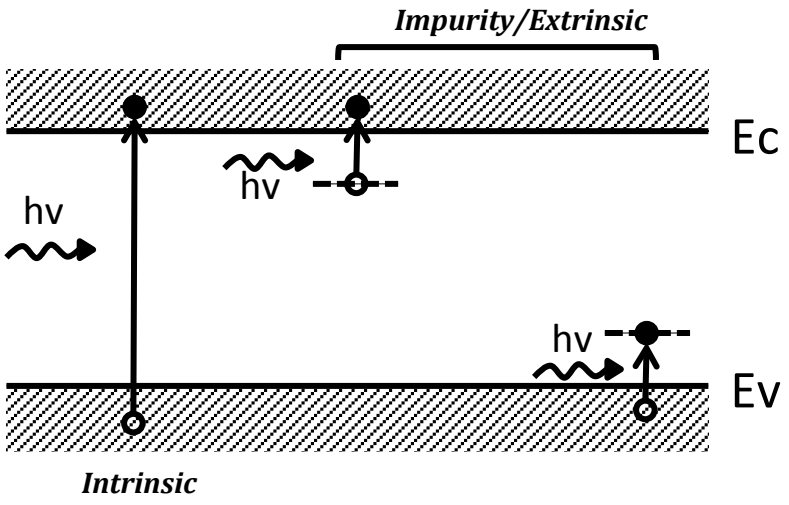

Figure 1 – Carrier energy level transitions.

Photoconductors have several advantages over other photodetector architectures. The processing steps required to produce such a device are not significantly more complicated than those required to produce a resistor. The speed of the device is mainly a function of the carrier transit time as a result of the cathode and anode separation; therefore an increase in bandwidth may be achieved by reducing the contact spacing.

A photoconductive detector is generally made up of a conducting cathode and anode attached to a bulk or film semiconductor with an absorption edge at at least the

desired incident photon energy. This absorption edge occurs in germanium at a photon energy of 0.8 eV corresponding to a wavelength of approximately 1550 nm, as shown in fig. 2. The germanium absorption edge is ideal, since it nearly corresponds to the standard communications wavelength at 1550 nm.

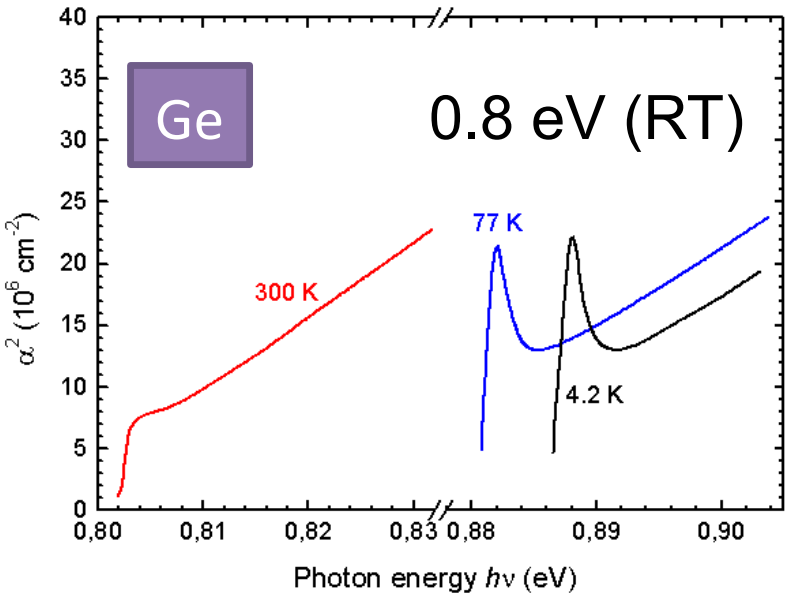

Figure 2 - Absorption spectra of germanium at various temperatures. Credit: (http://www.ioffe.ru/SVA/NSM/Semicond/Ge/bandstr.html).

Photoconductive detectors are so named for their reaction to optical stimuli. The conductivity of an intrinsic semiconductor may be expressed as

$$\sigma = q(\mu_n n + \mu_p p)$$

where 'q' is the electronic charge in Coulombs, 'μ_n' is the electron mobility, 'μ_p' is the hole mobility in square centimeters per volt-second and 'n' and 'p' are the electron and hole carrier concentrations in units of per cubic centimeter, respectively. A photon flux incident upon the photoconductor will cause a change in the carrier concentration $(\delta n, \delta_p)$.

$$\sigma = q\left(\mu_n(n + \delta n) + \mu_p(p + \delta p)\right)$$

The excess carrier concentration may be expressed in terms of the excess minority carrier lifetime 'τ' and generate rate 'G_L'

$$\delta n = G_L \tau_n$$

$$\delta p = G_L \tau_p$$

We can express the generation rate as the ratio of the carrier concentration rate to the carrier concentration or in terms of the photon flux

$$G_L = \frac{n}{\tau} = \frac{\eta\left(\frac{P_{opt}}{h\nu}\right)}{WLD} \qquad \text{Eq. 1}$$

where 'η' is the quantum efficiency (the number of electron holes generated per photon). This expression may be simplified by realizing that the excess carrier concentrations must be equal for electrostatic equilibrium.

$$\sigma = q\left(\mu_n n_0 + \mu_p p_0\right) + q(\delta n)\left(\mu_n + \mu_p\right)$$

Here, the first term is clearly the semiconductor conductivity while the second term may be described as a net change in the conductivity as a result of optical excitation:

$$\Delta\sigma = q(\delta n)\left(\mu_n + \mu_p\right)$$

One may then consider the current density associated with this device. This quantity may be decomposed into two parts: a steady state current density and an excitation current density,

$$J = J_0 + J_L = E(\Delta\sigma + \sigma_0)$$

where 'J_0' is the steady state current density, 'J_L' is the change in current density due to illumination and 'E' is the applied electric field. Examining just the illuminated current density, we may arrive at a useful expression for the illuminated current

$$I_L = J_L \cdot A$$

$$= E \cdot A \cdot [\Delta\sigma]$$

$$= E \cdot A \cdot \left[\delta n(\mu_n + \mu_p)q\right]$$

$$= q \cdot E \cdot A(G_L\tau_n)(\mu_n + \mu_p)$$

$$= q \cdot \eta \cdot \left(\frac{P_{opt}}{h\nu}\right)(\mu_n + \mu_p)\tau\left(\frac{E}{L}\right)$$

For sufficiently high electric fields, this expression will result in a nearly linear current-voltage characteristic.

2.2 Responsivity

Having calculated the photocurrent for a photoconductor, we may now examine a critical metric associated with these devices. Responsivity quantifies the conversion of optical power to electrical current, in units of Amperes per Watt. It is defined as the ratio of the illumination induced current in Amperes to the input optical power in Watts.

$$R = \frac{I_L}{P_{opt}} = \frac{q \cdot \eta \cdot \left(\frac{P_{opt}}{h\nu}\right)(\mu_n + \mu_p)\tau\left(\frac{E}{L}\right)}{P_{opt}}$$

Simply by knowing the wavelength of the incident light, one can calculate the theoretical maximum photoexcitation that can occur in the absence of gain. This is known as unity quantum efficiency and is expressed in the following manner.

$$\eta = \frac{\Phi_{electron}}{\Phi_{photon}} = \frac{\left(\frac{I_L}{q}\right)}{\left(\frac{P_{opt}}{h\nu}\right)} = \frac{q\lambda}{hc}$$

For 1550 nm radiation, we have that unity quantum efficiency corresponds to approximately 1.25 Amperes per Watt.

2.3 Dark Current

In addition to responsivity, dark current is a critical figure of merit. It describes the amount of current passing through the device under bias without illumination.

$$I_0 = EA\sigma_0 = EAq\left(\mu_n n_0 + \mu_p p_0\right)$$

In order for a system involving photodetection to be low power, this number should be minimized with low conductivity semiconductor materials. Large dark currents also contribute significantly to the minimum detection level of a photodetector as will be explored in detail, later.

2.4 Gain

It is possible to exceed unity quantum efficiency in a photoconductive detector via a mechanism called photoconductive gain. Conceptually, when a photon is incident upon the germanium lattice, an electron hole pair is generated. The electron and hole may travel at differing saturation velocities. One can readily imagine a scenario where the electron reaches the positive contact before the hole reaches the negative contact. At least temporarily, a non-electrostatic equilibrium condition is reached. Assuming current injecting contacts, an electron will be injected in order to regain the equilibrium state. Thus, one photon may result in multiple carriers reaching the contact.

Mathematically, we can describe this scenario as the ratio of the aggregate photocurrent I_L to the primary photocurrent I_{Lp}.

$$G = \frac{I_L}{I_{Lp}} = \frac{\mu_n + \mu_p}{L}\tau E = \tau\left(\frac{1}{t_{rn}} + \frac{1}{t_{rp}}\right)$$

Here, t_{rn} and t_{rp} are the electron and hole transit times, respectively. Examining the preceding equation, there is a clear trade-off between speed and gain.

Chapter 3. Design of Device

3.1 Materials

In communications, the standard wavelength has been chosen as 1550 nm for several reasons. The first being the absorption spectra of one of the most abundant compounds on Earth: SiO_2 or Silica. At 1550 nm, a local minimum in the absorption spectra exists in Silica. In order for an efficient waveguide to be built and enable modal coupling of light into a photodetector, it must be possible to achieve high index contrast with low absorption. At 1550 nm, silicon is quite up to the task of functioning as a high index modal confinement layer, or core. Conveniently, germanium both has high index contrast and high absorption at 1550 nm. For these reasons, a Ge layer was epitaxially grown on a Si waveguide atop a thick film of SiO_2.

3.2 Device Dimensions

The dimensions of a device affect both the manufacturing costs associated in its large-scale production as well as the operating frequency. There are many considerations when choosing the dimensions of an integrated photodetector and coupling waveguide. In the figure below, the selected device dimensions are displayed. Based on the dimensions in fig. 3, various hypotheses may be made via simulation and hand calculation regarding how it will perform.

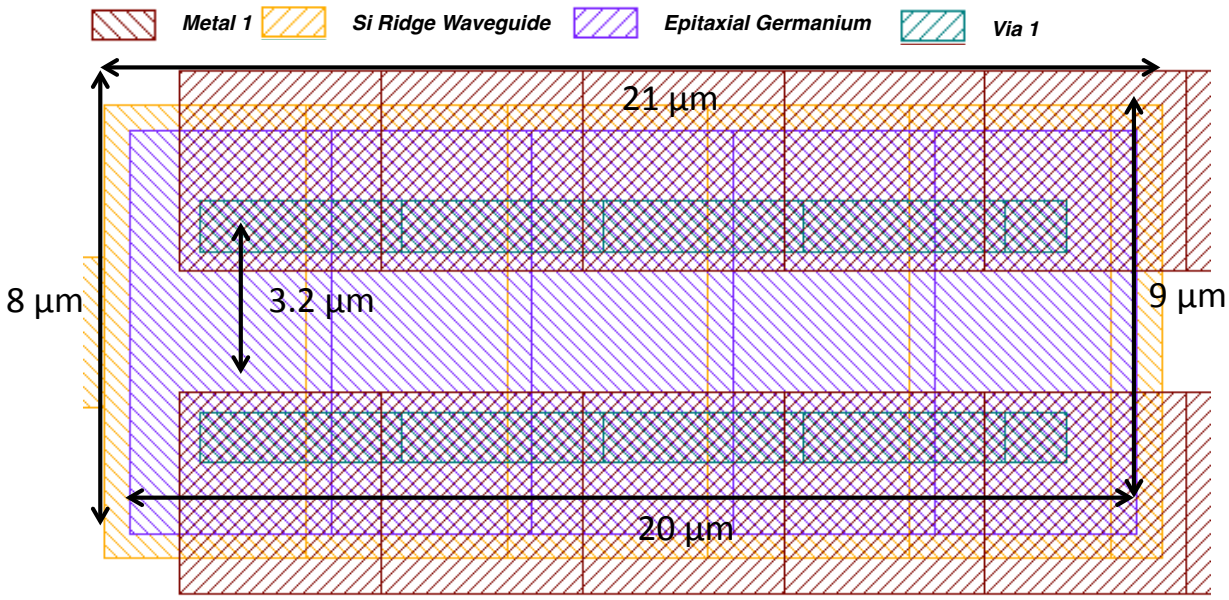

Figure 3 – Layout and dimensions of the photoconductive detector.

3.3 Responsivity

The length of the photodetector structure is rather important in determining the responsivity. Beer's law may be used to model the spatial absorption behavior of the absorbing germanium layer, that is to say, a decaying exponential function. If the optical mode does not decay to nearly zero after having gone the length of the waveguide, the photodetector will not have absorbed all of the possible radiation. This reduces the overall responsivity of the device and is highly undesirable. In the case of minimizing parasitic capacitance and resistance, it may be desirable to have a short device. However, one would be sacrificing responsivity for bandwidth. Here, a length of 20 µm was designed for in order to ensure complete absorption.

3.4 Bandwidth

Carrier transit time is one of the limiting factors in determining the operational frequency of a photodetector. In general, the closer the cathode and anode are placed, the

shorter the carrier transit time. For longitudinal parallel contacts, the width of the photodetector will be determined by manufacturing process capability. A contact spacing of 3.2 µm was chosen, as shown in the figure above so as to provide a reasonable bandwidth as well as pad the minimum dimensions of the process and make the functionality of the device on the first manufacturing attempt more likely. Assuming an electron saturation velocity of $6 \cdot 10^4 \frac{m}{s}$, we have the following bandwidth prediction for the device based on the transit time alone.

$$BW = 0.45 \frac{1}{t_n} = 0.45 \frac{V_{n_{sat}}}{L} = 0.45 \frac{6 \cdot 10^4 \frac{m}{s}}{3.2\ \mu m} = 8.55\ GHz$$

3.5 Capacitance

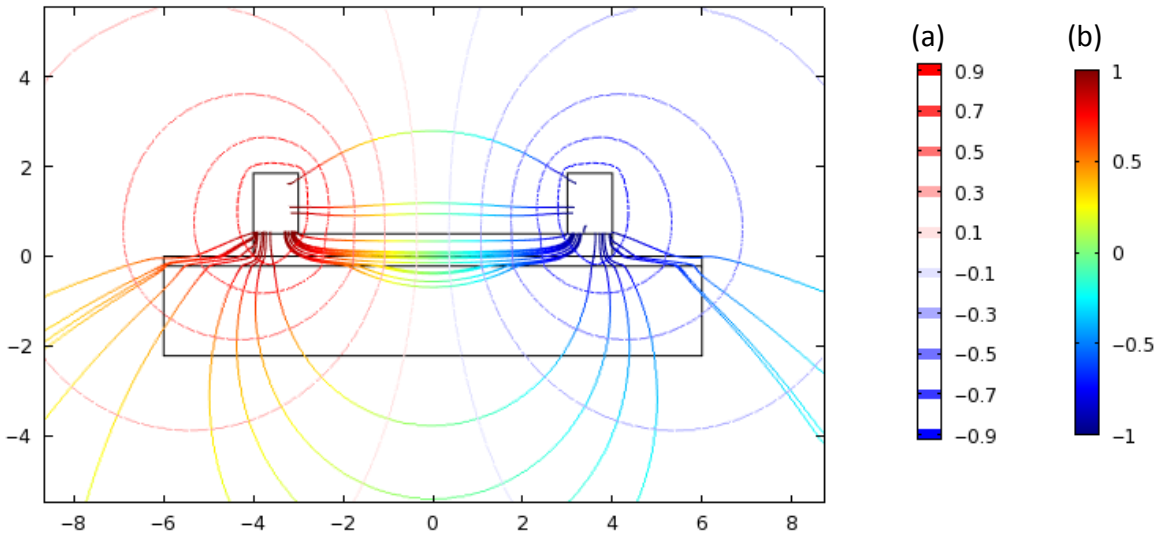

Figure 4 – Results of a COMSOL simulation of the photoconductive detector structure. The contour color bars denote the two data types shown (a) the electric potential and (b) normalized electric field distribution.

COMSOL was used to simulate the photoconductive detector design in two dimensions. The via metal layer width was set to 1 µm with a thickness of 0.6 µm, the silicon waveguide layer was set to 220 nm thick and 9 µm wide and the germanium layer was set as 8 µm wide and 0.5 µm thick. A capacitance per length was extracted from the

simulation, specifically 10 pF/m. For a 20 μm photodetector, this results in a very small capacitance of 0.2 fF. As can be readily seen in the figure above, the electric field is largely concentrated in the germanium layer. With a dielectric constant of 16.0, the germanium lattice responds readily to the applied field, storing energy and behaving as a leaky capacitor. The metal contacts contribute significantly less to the overall device capacitance, as can be seen in the figure above.

3.6 Cavity Modes

In order for a specific waveguide and photodetector pair to function, a mode or modes must be supported at the wavelength of the incident light. If a mode is not supported at this wavelength, the light will not propagate. Instead, the fields will evanesce as a function of the distance over which the light penetrates into the waveguiding structure.

In order to determine if a mode is supported, one must examine the set of equations describing electromagnetic radiation: Maxwell's equations. Consider the charge-free EM curl equations:

$$\nabla \times H = \frac{\partial}{\partial t} \epsilon E$$

$$\nabla \times E = -\frac{\partial}{\partial t} \mu H$$

We may then assume an exponential time dependence of $e^{-i\omega t}$, eliminating the temporal differentials.

$$\nabla \times H = -i\omega \epsilon E$$

$$\nabla \times E = i\omega \mu H$$

Left multiplying by the inverse permittivity distribution, taking the curl of both sides and using Maxwell's electric curl equation we arrive at an EM eigenproblem expression.

$$\nabla\times\frac{1}{\epsilon(\boldsymbol{r})}\nabla\times H = -i\omega(\nabla\times E)$$

$$= -i\omega(i\omega\mu)H$$

$$= \mu\cdot\omega^2 H$$

The left hand side operator is, in fact, Hermitian. Hermiticity implies that the following relation holds.

$$< \psi_a|A|\psi_b >=< \psi_b|A|\psi_a >^*$$

More specifically, we can say the following must be true for the Hermitian operator described by Maxwell's magnetic eigenproblem.

$$\int H_a^*\cdot\left(\nabla\times\frac{1}{\epsilon}\nabla\times H_b\right)dV = \int\left(\nabla\times\frac{1}{\epsilon}\nabla\times H_a^*\right)\cdot H_b dV$$

Operator hermiticity and sparseness are immensely beneficial in computational physics due to the number of efficient eigenproblem algorithms that have been developed for this class of problem.

The Lanczos algorithm enables solving of the extremal eigenvalues and eigenvectors of large sparse Hermitian operators. It draws its efficiency from its ability to perform eigenproblem calculations on the Krylov subspace associated with the double curl operator, as opposed to the full operator space. Conveniently, it can be shown that the eigenvalues of the Krylov subspace found during the Lanczos algorithm are approximately the eigenvalues of the operator. This reduces the matrix dimensionality from hundreds of thousands of entries, resulting in memory requirements that are not physical, to hundreds of entries.

The convergence of Lanczos' algorithm is somewhat surprising, but it may be understood by examining the optimization of the Rayleigh quotient.

$$r(x) = \frac{x^T A x}{x^T x}$$

It can be shown that the maximum and minimum eigenvalues of the operator matrix A are the maximum and minimum values of $r(x)$, respectively. Let $Q_i = [q_1, \dots, q_k]$ be a set of orthonormal vectors. We may then define the scalar quantities O_k and o_k.

$$O_k = \lambda_1(Q_k^T A Q_k)$$

Evaluating the Rayleigh quotient for the decomposition operator $Q_k^T A Q_k$ we have the following.

$$O_k = \max_{z \neq 0} \frac{z^T (Q_k^T A Q_k) z}{z^T z}$$

This may be re-expressed as a function of the Rayleigh quotient.

$$r(Q_k z) = \frac{(Q_k z)^T A (Q_k z)}{(Q_k z)^T (Q_k z)} = \frac{(Q_k z)^T A (Q_k z)}{|Q_k z|^2} \leq \frac{z^T (Q_k^T A Q_k) z}{z^T z}$$

$$\Longrightarrow O_k = \max_{||z||_2} r(Q_k z) \leq \lambda_1(A)$$

Using nearly identical reasoning, but this time minimizing the Rayleigh quotient we may come up with an inequality describing o_k.

$$o_k = \min_{||z||_2} r(Q_k z) \geq \lambda_n(A)$$

The goal of Lanczos algorithm will be to generate q_k such that O_k and o_k are increasingly accurate estimates of $\lambda_1(A)$ and $\lambda_n(A)$. We may examine some vector $y_k \, \epsilon \, span\{q_1, \dots, q_k\}$ such that $O_k = r(y_k)$. Now taking the gradient enables following the increasing direction of the Rayleigh quotient…

$$\nabla r(x) = \frac{2}{x^T x}(Ax - r(x)x)$$

To ensure the ascending order of O_k we may determine q_{k+1} such that the following holds.

$$\nabla r(y_k) \epsilon\ span\{q_1, \dots, q_{k+1}\}$$

If $u_k \epsilon\ span\{q_1, \dots, q_k\}$ satisfies $r(u_k) = o_k$, we may impose a similar requirement on the gradient of u_k as compared to the gradient of y_k.

$$\nabla r(u_k) \epsilon\ span\{q_1, \dots, q_{k+1}\}$$

Recall that u_k corresponds to the minimization of the Rayleigh quotient yielding an approximation to the largest eigenvalue of the operator matrix A. Next, an orthonormal vector q_{k+1} must be found that satisfies both gradient conditions $(r(y_k), r(u_k))$. Since $\nabla r(x) \epsilon\ span\{x, Ax\}$, we may satisfy both conditions if the following is true.

$$span\{q_1, \dots, q_k\} = span\{q_1, Aq_1, \dots, A^{k-1}q_1\}$$

$$\Longrightarrow span\{q_1, \dots, q_{k+1}\} = span\{q_1, Aq_1, \dots, A^{k-1}q_1, A^k q_1\}$$

Thus, we are left to compute an orthonormal basis for the Krylov subspace.

$$K(A, q_1, k) = span\{q_1, Aq_1, \dots, A^{k-1}q_1\}$$

It can be shown that the preceding relation describes the range spaces of the Krylov matrices.

$$K(A, q_1, n) = [q_1, Aq_1, \dots, A^{n-1}q_1]$$

Recall the tri-diagonal decomposition $Q^T AQ = T$ where $q_i = Qe_i$ where e_i is a unit identity vector. We may then compute the QR factorization of the Krylov range space.

$$K(A, q_1, n) = Q[e_1, Te_1, \dots, T^{n-1}e_1]$$

The extremal eigenvalues of T are approximately the eigenvalues of the original operator A. Calculating the eigenvectors of the tri-diagonal matrix T and then left multiplying by the set of orthonormal vectors Q_k produces the eigenvector of the original operator A.

The eigenvalue solved for in the case of the electromagnetic cavity eigenproblem discussed here happen to correspond to the modal frequency, ω after some minimal extraction. Namely,

$$\lambda_{mode} = \omega^2\mu \rightarrow \omega = \sqrt{\frac{\lambda_{mode}}{\mu}}$$

The Lanczos algorithm, as described, was implemented in C with the primary difference between the description here and the code manifesting in the normalization of Maxwell's equations. Implementing this algorithm required creation of a custom matrix calculation library, complex number library, electromagnetics operator library and eigenvector IO library.

3.6.1 Waveguide Mode

Solving the eigenproblem for a 400 nm by 200 nm ridge waveguide yields critical information such as the field distribution, modal effective index, and free space wavelength of the propagating mode. In fig. 3 the waveguide dimensions are visible via a spatial contour plot of the index of refraction representing each material used in the waveguide construction.

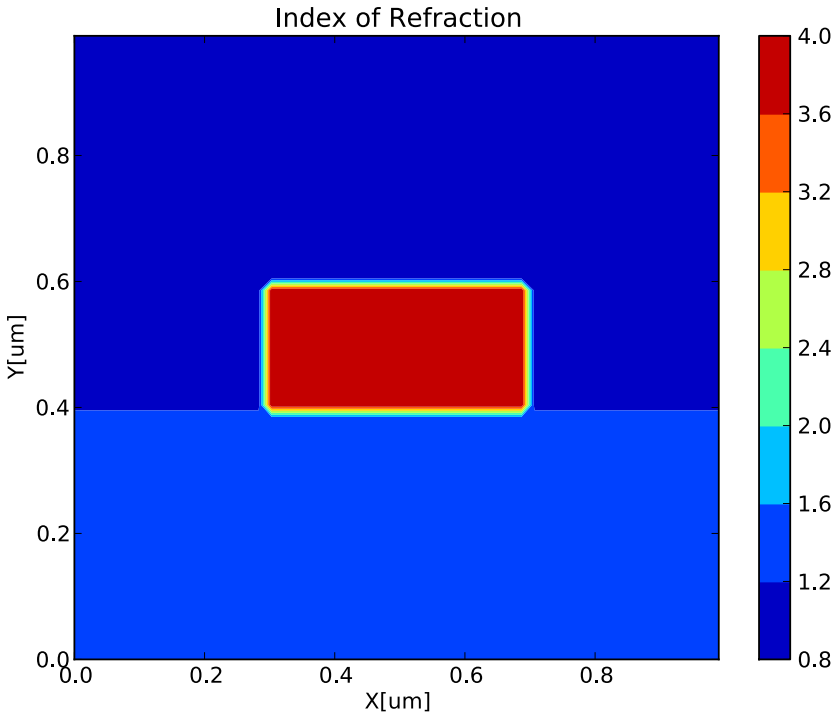

Figure 5 - Contour plot of the index of refraction distribution for an air clad (n=1), silicon core (n=3.96) and silicon dioxide (n=1.46) substrate waveguide measuring 200 nm in height by 400 nm in width.

Examining the electric field and magnetic field distributions in fig. 4, they are clearly confined spatially within the waveguiding structure. The mode in fig. 4 is supported at approximately 1550 nm with the following modal effective index, which is the ratio of the propagation constant β to the free space wavenumber k_0.

$$n_{eff} = \frac{\beta}{k_0} = \frac{10.5\ \mu m^{-1}}{4.04\ \mu m^{-1}} = 2.6$$

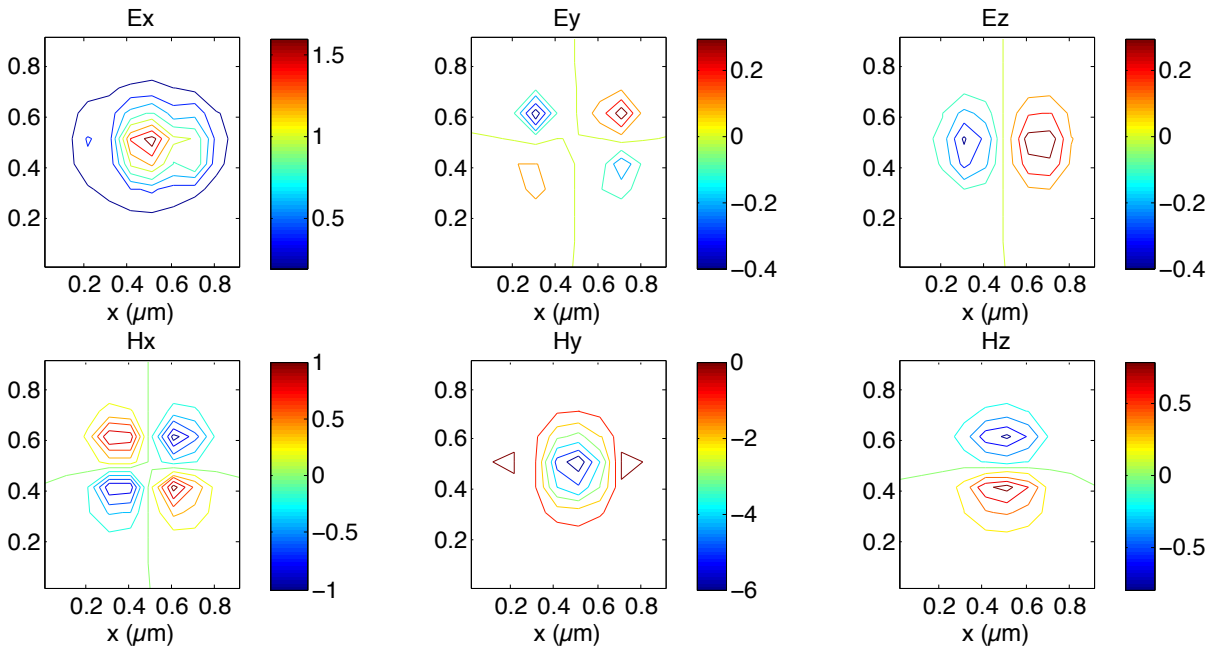

Figure 6 - Contour plots of the normalized electromagnetic field distributions within the waveguide structure.

Taking advantage of the eigensolver program developed to solve for the field distributions, the seed wavenumber may be changed resulting in modes being supported at different wavelengths. For a sufficiently extremal wavenumber, a mode will no longer be supported. This will be clear via plotting the mode simulation result, the field distributions, because they will be largely unconfined within the waveguiding structure. Varying the seed wavenumber in the Lanczos eigensolver and tracking the same mode profile results in a dispersion curve for the mode. This data is shown in fig. 5.

Here we can see the actual simulation data for the effective index as a function of the mode wavelength. The simulated data has been fit with a second order polynomial. A second order polynomial fit is convenient, since group velocity dispersion is defined as a second order differential of the index with respect to the wavelength. The expression for group velocity dispersion is as follows,

$$D = -\frac{\lambda}{c}\left(\frac{d^2n}{d\lambda^2}\right)$$

The second order coefficient for the simulation fit in fig. 5 was extracted. Performing the trivial multiplications entailed by the group velocity dispersion relation, we have that the value for D is 2.1E-3 ps per nm per km. Since D is positive, it is said to have negative or anomalous dispersion. This means that the high frequency components of an incident pulse composed of many wavelengths travel faster than the lower frequency components.

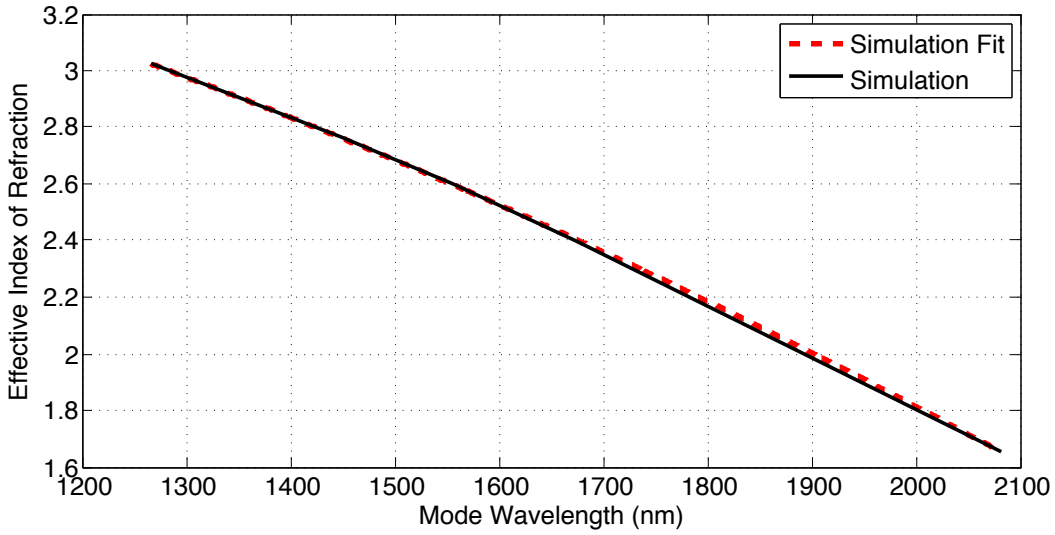

Figure 7 - Dispersion diagram for TE0 mode of a 400 nm by 200 nm silicon waveguide clad in air and built on a silicon dioxide layer. A quadratic fit of the simulated dispersion curve is also supplied.

3.6.2 Photodetector Mode

In fig. 6, the index of refraction distribution is shown for the photodetector structure. Larger cavities support more modes since there are more possible solutions to Maxwell's equations in such a case. The structure in fig. 6 is highly multi-modal.

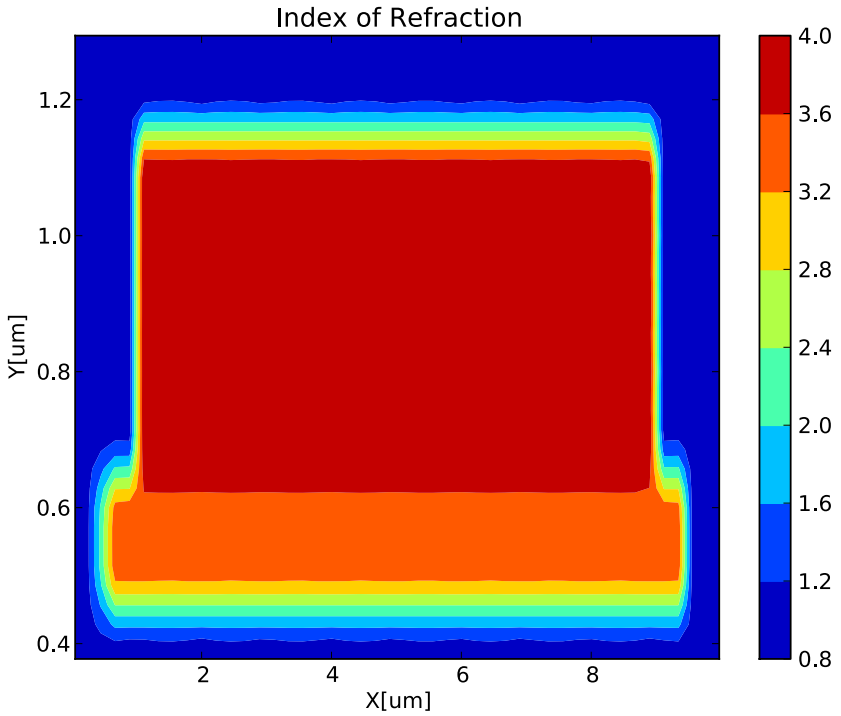

Figure 8 - Contour plot of the index of refraction distribution for the photodetector structure. The 500 nm by 8 µm germanium layer sits atop a silicon slab waveguide measuring 9 µm wide by 220 nm tall.

A photodetector mode was solved for in a similar fashion as for the waveguide mode, as shown in fig. 7. In fig. 7, it is clear that the light is largely confined to the germanium slab. In order for light to couple between the waveguide and photodetector and not be ejected at the interface, the refractive indices must match somewhat. Luckily, the modes existing in the germanium and silicon have quite similar effective refractive indices—thus significant scattering will not occur. A steadily widening taper on the input waveguide is used to expand the optical mode to the spatial extent of the germanium layer for maximal absorption.

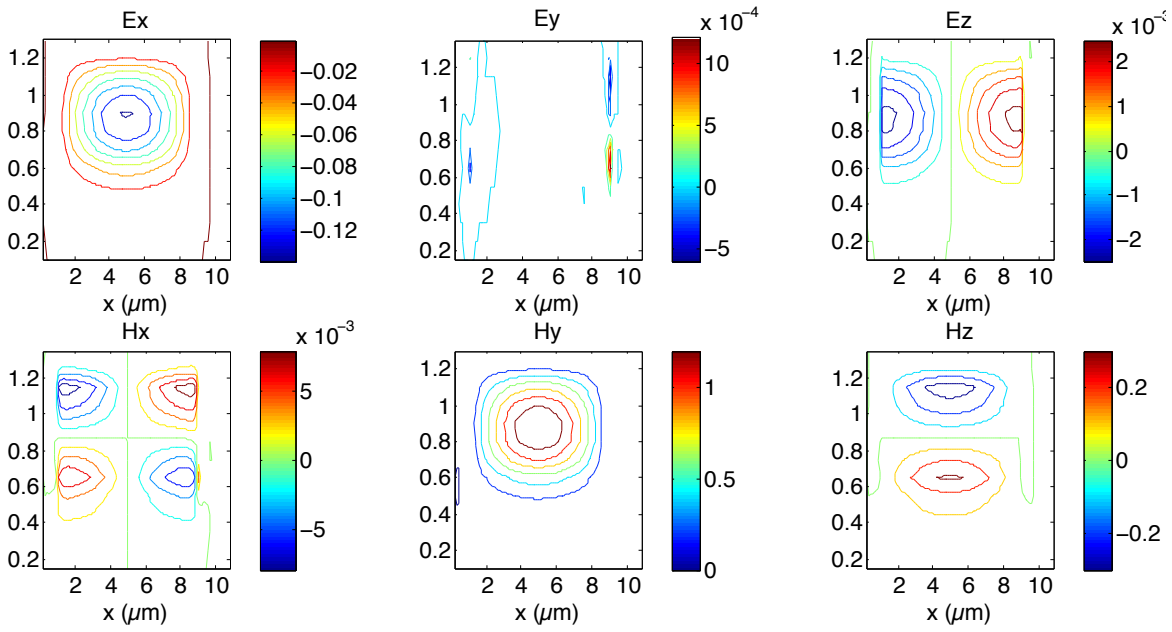

Figure 9 - Photodetector electric and magnetic field distributions resulting from simulation.

The incident waveguide optical mode has a lesser spatial extent than the germanium film that it is coupled to, thus approximately all of the power will be transferred. It is not necessary that the germanium layer actually guide light, since the goal is absorption within the structure.

3.6.3 Modal Coupling

Knowing the modal profiles for the waveguide and photodetector, it is possible to determine the amount of loss associated with entry of the mode into the photodetector from the waveguide. First the fields are normalized such that the modal power is unity. For this to be true, the A-norm below must hold.

$$c^2 \cdot < \psi | A | \psi >= 1$$

Where the operator A and vector EM 6-vector ψ are given as below, and 'c' is a complex normalization constant.

$$A = \begin{bmatrix} 0 & 0 & 0 & 0 & 1 & 0 \\ 0 & 0 & 0 & -1 & 0 & 0 \\ 0 & 0 & 0 & 0 & 0 & 0 \\ 0 & -1 & 0 & 0 & 0 & 0 \\ 1 & 0 & 0 & 0 & 0 & 0 \\ 0 & 0 & 0 & 0 & 0 & 0 \end{bmatrix}; \ \psi = \begin{bmatrix} Ex \\ Ey \\ Ez \\ Hx \\ Hy \\ Hz \end{bmatrix}$$

To normalize the mode, the modal profile must be multiplied by the constant 'c'. Next, we can calculate the modal power-coupling coefficient that describes the optical power coupling efficiency via the following inner product space relation:

$$\eta_{opt} = |< \psi_{PD}|A|\psi_{WG} >|^2$$

where ψ_{PD} is the photodetector cavity mode and ψ_{WG} is the waveguide cavity mode.

Chapter 4. Overview of Noise Mechanisms

4.1 Relevance of Noise in Photodetection

The noise floor of a system describes the minimum power level at which a signal may still carry information and is the point at which the signal to noise ratio of a system is one to one. In the case of a photodetector, the noise floor and responsivity of the device determine the minimum amount of optical power required for optical to electrical transduction. In applications such as single photon detection, achieving low noise is critical.

4.2 Shot Noise

4.2.1 Conceptual Description

Electrons incident upon a potential barrier will be either transmitted or reflected. A photon incident upon a crystalline lattice such as Ge may be absorbed and generate an

electron hole pair with the electron being excited to the conduction band, or not. Shot noise is the result of many events with binomial outcomes. Since events are random and independent, Poisson statistics apply.

4.2.2 Derivation

As shown by van der Ziel, one may derive the expression quantifying shot noise from first principles. Let $\phi(t)$ be the carrier flux rate and Φ be the number of carriers passing a point over some time interval τ, then the following is intuitive

$$\Phi = \int_0^\tau \phi(t) \cdot dt$$

Using the Ergodic theorem, we can say that the time average of $\phi(t)$ is equivalent to the ensemble average in this case,

$$\overline{\Phi} = \bar{\phi}\tau$$

We may now consider only small changes in Φ by discounting the ensemble average,

$$\Delta\overline{\Phi} = \Phi - \overline{\Phi}$$

Defining a random process X_τ,

$$X_\tau = \frac{\Delta\Phi}{\tau}$$

For a Poisson process such as this,

$$var(\phi) = \bar{\phi}$$

$$var(\Phi) = \overline{\Phi} = \overline{\Delta\Phi^2}$$

Squaring both sides of the random ensemble process $\overline{X_{tau}}$

$$\overline{X_\tau^2} = \frac{\overline{\Delta\Phi^2}}{\tau^2} = \frac{\overline{\Phi}}{\tau^2} = \frac{\bar{\phi}\tau}{\tau^2} = \frac{var(\phi)}{\tau}$$

$$\Rightarrow var(\phi) = \tau\overline{X_\tau^2}$$

Employing the Wiener–Khinchin Theorem to calculate the power spectral density of the random process $\overline{X_\tau^2}$

$$S_\phi(f) = \lim_{\tau\to\infty} \tau\overline{X_\tau^2} = var(\phi)$$

Now, consider the electrical current by multiplying by the electronic charge 'q',

$$I(t) = q\phi(t) \rightarrow \bar{I} = q\bar{\phi}$$

The power spectral density of current may then be calculated

$$S_I(f) = q^2 S_\phi(f) = 2q^2 var(\phi) = 2q^2\bar{\phi} = 2q\bar{I}$$

with units of squared-Ampere seconds.

4.2.3 Spectral Characteristic

The final result obtained is that Shot noise is frequency independent and the result of independent binomial events.

$$S_I = S_{shot} = 2qI_{DC}$$

4.2.4 Circuit Model

Examining the units of the Shot noise power spectral density serves as a useful tool in modeling this type of noise as a circuit element—specifically a current source.

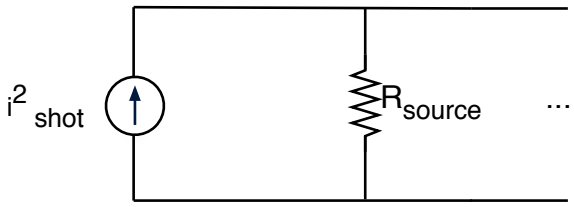

Figure 10 - Equivalent circuit representing the shot noise contribution resulting from the Boolean outcome probabilistic flow of carriers across a potential barrier.

4.3 Thermal Noise

4.3.1 Conceptual Description

Thermal noise in resistors is the result of the random motion of electrons as they interact with phonons. The phonon power spectral density is the available noise power in a resistor.

4.3.2 Derivation

The Bose-Einstein occupation factor is given as,

$$\overline{n_i} = \frac{1}{e^{\frac{\hbar\omega_i}{k_B T}} - 1} + \frac{1}{2}$$

Since the phonon energy is in harmonic oscillator units,

$$E_s = \hbar\omega_s \left(n_s + \frac{1}{2}\right);\ n_s = 0,1,2,\ldots$$

we may re-express this, account for the Bose-Einstein occupation factor and invoke Nyquist's Theorem. Nyquist's Theorem states that the phonon power spectral density is the available electrical noise power in a resistor.

$$E_i = \hbar\omega_i \left(\frac{1}{e^{\frac{\hbar\omega_i}{k_B T}} - 1} + \frac{1}{2}\right) = S_{phonon}$$

In the case where $\hbar\omega \ll k_B T$,

$$S_{phonon} = \lim_{\hbar\omega_i \to 0} \frac{\hbar\omega_i}{e^{\frac{\hbar\omega_i}{k_B T}} - 1} = k_B T$$

in units of Watts per Hertz. Although obvious from the preceding relation, it is important to emphasis that the available phonon power spectral density may be modulated with temperature. Below, this relationship has been plotted.

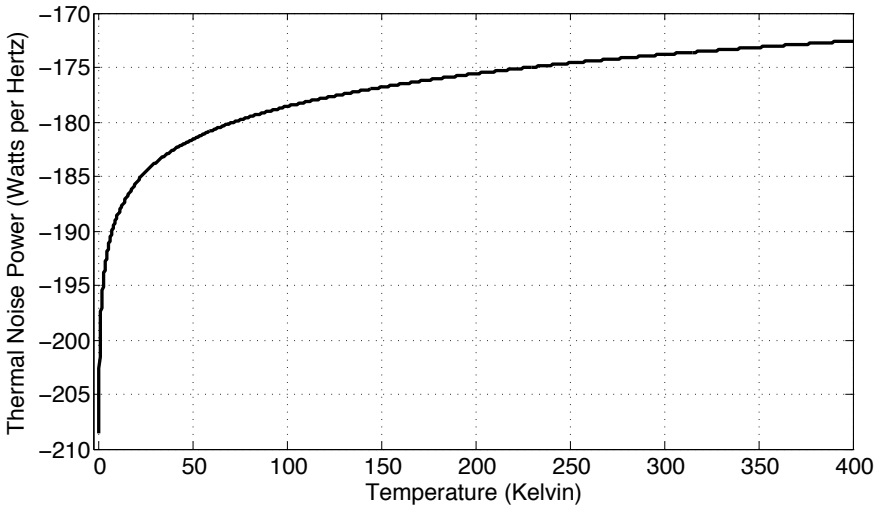

Figure 11 - Plot of the thermal noise power for various temperatures.

Note that, at room temperature, the noise floor will always be at least -174 dBm per Hz. In order to measure noise below this limit at 300 K, it is necessary to cool the device under test as well as the measurement equipment.

4.3.3 Circuit Model

Just as in the case of shot noise, it is useful to model thermal noise as a circuit element. Examining the power spectral density units, Watts per Hertz, one can quickly determine the power delivered to a matched load impedance 'R' where a lowercase 'i' is used to denote a spectral current.

$$P_{load} = \frac{i}{2}V = \frac{i^2}{2^2}R \rightarrow k_B T = \frac{i^2}{2^2}R \Rightarrow i^2 = S_{thermal} = \frac{4k_B T}{R}$$

To accurately model thermal noise, the noise power current source is placed in parallel with the resistor generating the thermal radiation.

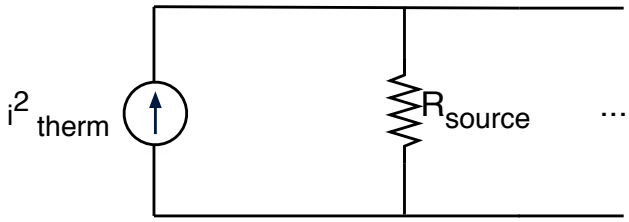

Figure 12 - Equivalent circuit representing the noise contribution of a resistor in terms of a spectral noise current.

4.4 Flicker Noise

4.4.1 Conceptual Description

Flicker noise has no general theoretical origin, however, there are several potential contributors to this type of noise including valence band discontinuity in Ge-Si devices, large defect densities and contact processing. The defining characteristic of flicker noise is its proportionality to the aggregate direct current flowing through the device. The figure of merit associated with flicker noise is known as the noise elbow. This is the frequency at which the noise is mostly dominated by the spectrally white noise mechanisms: shot and thermal noise.

4.4.2 Spectral Characteristics

Unlike shot noise and thermal noise, flicker noise varies in magnitude as the inverse of frequency. Of course, infinite noise power at zero Hertz is non-physical and will not be realized in a practical system. Flicker noise spectral density is generally fit with the following functional form where 'a', 'K_f', and 'γ' are curve fitting factors.

$$S_{flicker} = K_f \cdot \frac{I_{DC}^{a}}{f^{\gamma}}$$

Chapter 5. Fabrication

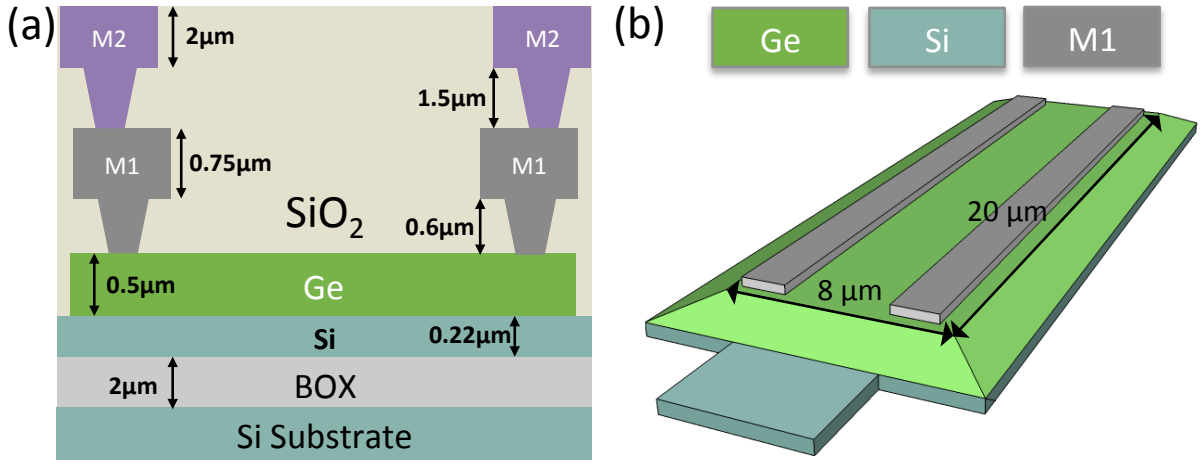

Figure 13 - MSM photodetector fabrication specifications. (a) Cross-sectional view of process stack for detector. (b) Schematic view of detector.

The MSM detectors were fabricated at the Institute of Microelectronics (IME), Agency for Science Technology and Research (A*STAR), Singapore on an 8-inch SOI wafer with 220nm top silicon, 2µm buried-oxide, and a high resistivity silicon substrate [12]. The epitaxially grown germanium layer measured 8µm laterally, 20µm longitudinally and 500nm in thickness as shown in Fig. 11 (a) and (b). Thin germanium layers are beneficial as they reduce aggregate device capacitance as well as increase the volumetric penetration of the electric field into the germanium, resulting in drift-limited carrier transit times [5]. The 20µm detector germanium length, as shown in Fig. 11 (b), was selected to ensure near complete light absorption. Dopants were not applied beneath the Via 1 region, resulting in non-Ohmic contact, although the dark IV sweeps were linear over a range of at least -5V to 5V contact bias. Metal 1 and metal 2 were composed of a TaN/Al/TaN stack and an Al/TaN stack, respectively. The optical mode was coupled via a 500nm silicon ridge waveguide tapered to 3µm.

Chapter 6. Device Testing

6.1 Bandwidth, Responsivity and Dark Current

The critical device parameters were characterized including capacitance, bandwidth, dark resistance and responsivity. Bandwidth was measured by driving modulated light into the MSM photodetector using a 10GHz lithium niobate modulator acting on laser light at 1550nm and measuring the response with a vector network analyzer (VNA).

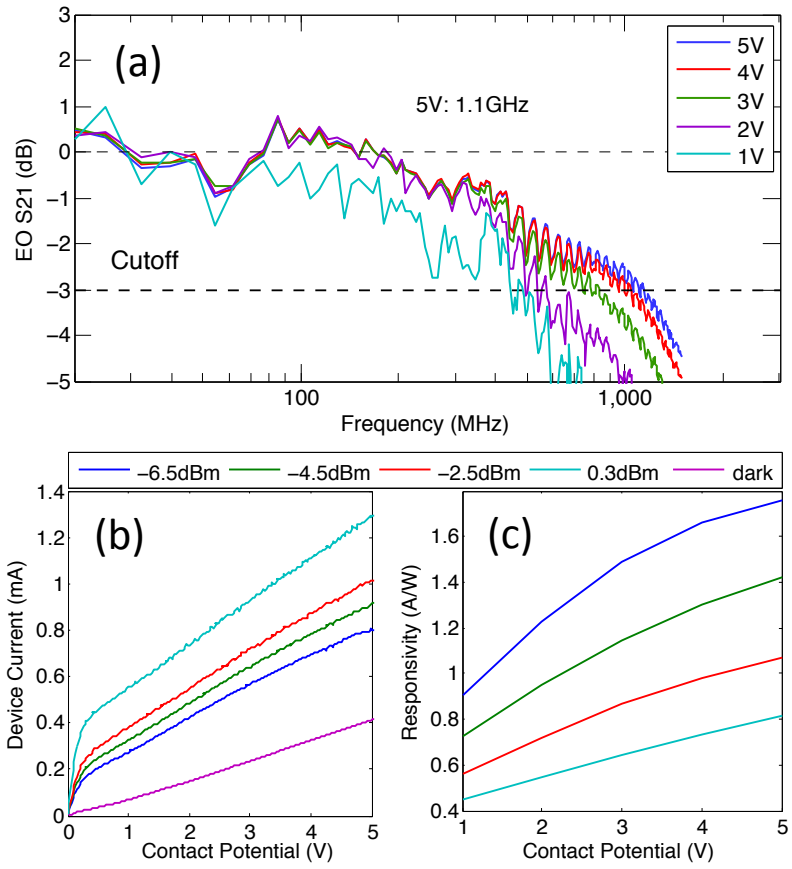

Figure 14 - MSM photodetector 3 dB bandwidth under various bias conditions, (b) IV characteristic and (c) responsivity under various illumination levels and contact potentials.

The device had a 3dB bandwidth of 1.1GHz at 5V contact bias as shown in Fig. 12 (a). A 3.2µm contact spacing resulted in this carrier transit time limited bandwidth. Assuming a

standard germanium electron saturation velocity of 6E4 m/s, the theoretical bandwidth would have been approximately 8.4 GHz [13]. The discrepancy is likely caused by defects in the Germanium growth decreasing the carrier saturation velocity [14]. Detector speed can be improved in the future by either improving Ge growth quality, or decreasing contact spacing.

The current-voltage characteristic of the MSM photodetector was recorded at various contact potentials using a semiconductor device analyzer (SDA). As shown in Fig. 12 (b), at 5V bias the dark current measured 412±1.07 μA, yielding a 12.17kΩ dark resistance—comparable to the dark resistance measured in [5]. Responsivity was then extracted from the IV curves at various potentials. As shown in Fig. 12 (c), unity quantum efficiency is exceeded by 41% at 1.76 A/W for 5V bias. There are two possible origins for this large responsivity: avalanche gain and photoconductive gain. Linearity in the IV curves as shown in Fig. 12 (b) serves as a good indicator that avalanche multiplication is not occurring. If it were, there would be an asymptotic current increase at higher contact potentials. This leads us to believe that photoconductive gain is the cause of the increased responsivity—a well-known mechanism that exists in certain material systems when the carrier lifetime is longer than the transit time and the contacts are current-injecting [15].

In order to determine the capacitance of the device, the argument of S11 was measured using a VNA under two conditions: (1) the RF GSG probe floating and (2) contacting a metal de-embedding structure with the same pad and metal configuration. These extraneous capacitances were normalized out of the device capacitance—resulting in a measured MSM photodetector capacitance of 10.6fF±0.96fF. This value is quite

close to the device capacitance reported by Assefa et. al in [5] and it results in a large RC bandwidth.

6.2 Noise Measurements

6.2.1 White noise

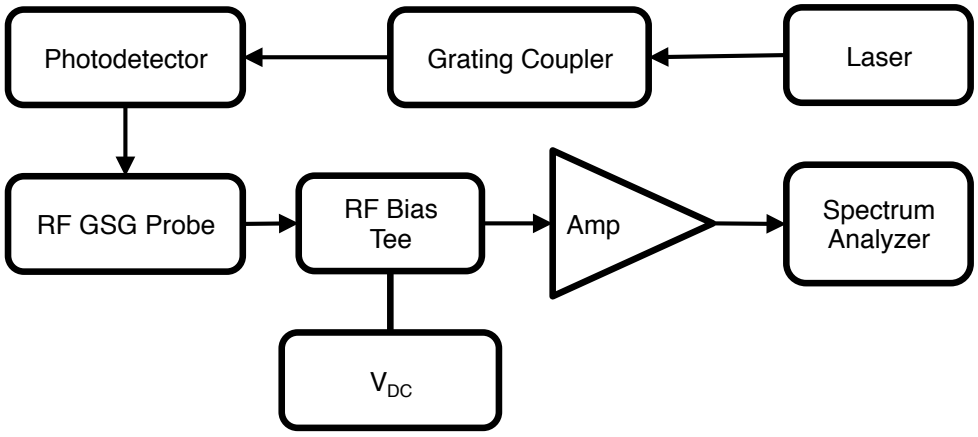

Figure 15 - White noise measurement apparatus.

The average laboratory temperature was measured at approximately 295 Kelvin. A Tektronix RSA6114A spectrum analyzer was used to measure the noise emitted by the photodetector. To improve the minimum detectable noise power, an external low-noise amplifier (LNA) with a gain of 35 dB and a noise figure of 4 dB was employed. To avoid introducing laser relative intensity noise (RIN) as a source of error in the noise measurements, all data was captured without illumination. The noise signal was routed from the photodetector through an RF GSG probe, bias tee with 0.7dB insertion loss, and external LNA in an SMA (50Ω) environment. The SMA environment imposes a detection limit of approximately -173.9 dBm/Hz at 295 K. The photodetector noise was measured over a broad spectral range for a 5V bias.

The measured noise may be interpreted as the sum of the noise generated by the photodetector and the noise generated by the LNA and bias tee. These noise quantities

are composed of spectrally dependent terms due to the flicker noise as well as spectrally constant terms due to shot and thermal noise. All noise from the bias tee and LNA can be considered as additional noise added before the first bias tee, with the bias tee and LNA then considered as noiseless RF components [11,18,19]. The net gain and noise figure of the bias tee/LNA system can be readily calculated as 34.3 dB and 4.7 dB, respectively. We then have:

$$P_{out}\left(f\right) = g\left(P_{DUT}\left(f\right) + \left(nf - 1\right)k_b T\right)$$

Here 'P_{out}' is the spectral distribution of RF power at the output of the bias tee and LNA system in W/Hz, 'g' is the gain in a linear scale (in this case 2691.5), 'P_{DUT}' is the spectral distribution of RF power emerging from the device under test, 'nf' is the linear noise factor (in this case 2.95), 'k_b' is Boltzmann's constant in mW/(K Hz) and T is temperature in K. In the case of a simple 50Ω resistor being measured, P_{DUT} would simply be k_bT.

Output power from the device, bias tee and LNA chain was taken in a number of situations. A resolution bandwidth of approximately 5 MHz was used, with the spectrum analyzer preamplifier enabled. The power reading given by the RSA was then divided by the resolution bandwidth, and then the net gain of the bias tee and LNA system, to yield the effective RF power at the input for 1 Hz bandwidth. A number of experiments were conducted. In one instance, the photoconductive detector was measured with 5V bias voltage. In another instance, the RF probes were pulled back from the device to break electrical contact, but the system was otherwise unchanged. In another instance, the RF probe and detector were replaced by a 50Ω resistor. The results of these experiments, with the aforementioned normalization performed, are shown in Fig. 4. We also plot the

Johnson noise prediction—the noise level that should have been seen, based on the noise figure from the bias tee and LNA system connected to a 50Ω termination resistor.

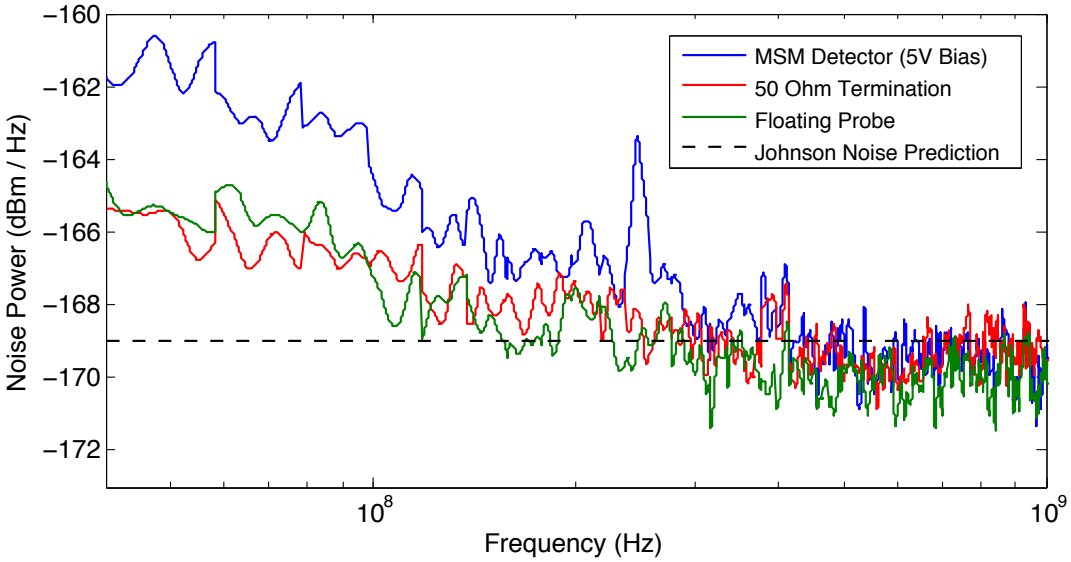

Figure 16 - MSM photodetector noise measured with 5 V bias, 50 Ω terminator control experiment, floating RF GSG probe control experiment and Johnson noise prediction.

It is immediately clear from Fig 14. that the noise emitted from all configurations is very similar at high frequencies. As expected, both the 50Ω terminator and the floating probe measurement result in identical levels of noise, nearly consistent with the Johnson noise prediction. The average noise is slightly lower than the Johnson noise prediction, which may be due to the amplifier having a slightly lower noise figure than reported at some frequencies. The detector noise also is nearly in agreement with these values at high frequencies, suggesting that minimal excess noise is being added by the shot noise mechanism. This is an interesting result, considering that the shot noise should have increased the device noise level by 159% in power. The predicted noise level that would be seen in Fig. 14, should be -167.2 dBm/Hz, if all of the dark current were associated with shot noise in Eq. (2). This is clearly substantially higher than the noise level seen in

Fig. 14 at high frequencies. We can thus conclude that at least a substantial portion of the dark current in the photodetector is not associated with shot noise.

As shown in Fig. 14, the measured photodetector noise at high frequencies is at the Johnson noise prediction level, or -169.2 dBm/Hz. Thus, a value for the spectral noise emitted by the MSM photodetector of -173.9 dBm/Hz may be calculated by subtracting the excess noise generated by the LNA and bias tee from -169.2 dBm/Hz. Assuming a responsivity of 1.76 A/W, we then have that the measured NEP is 5.1 $pW/Hz^{1/2}$ at 5V bias. We may compare this to an NEP value reported by C. T. DeRose et. al of 0.66 $pW/Hz^{1/2}$ [6]. Typical transimpedance amplifiers (TIA) have input impedances near 50Ω, making the measured thermal noise floor close to what will be achieved in practice. In addition, any photodetector coupled to a transmission line will have similar noise output power levels.

It is interesting to note that even with the high bias voltage and large dark current, the high-frequency noise power emitted by the photoconductive detector shows little deviation from the theoretical minimum value in a 50Ω environment. The shot noise current, in A^2/Hz, due to dark current in avalanche photodetectors is described by the following relation

$$\left\langle i_s^2 \right\rangle = 2qI_{dark}M^2F$$

where 'q' is the electronic charge, 'I_{dark}' is the dark current flowing through the device, 'M' is the avalanche gain, and 'F' is the excess noise factor [14]. The shot noise current in darkness generated by this MSM detector may be compared favorably against detectors that employ avalanche gain due to the 'M^2F' term in Eq. (5). Assuming an photodetector had an 'M' of 3.0, an impressive 'F' of 1.7 as in [9], and 'I_{dark}' of 50μA in

a 50Ω environment, the high-frequency dark noise floor due to shot noise would become -169.1 dBm/Hz rather than -173.9 dBm/Hz measured here. It remains to be seen as to whether this favorable level of noise can be obtained for higher bandwidths, and higher levels of gain. However, if it can be, it suggests that photoconductive detectors may become useful in optical systems where low-noise gain is required from the photoreceiver portion.

6.2.2 Flicker noise

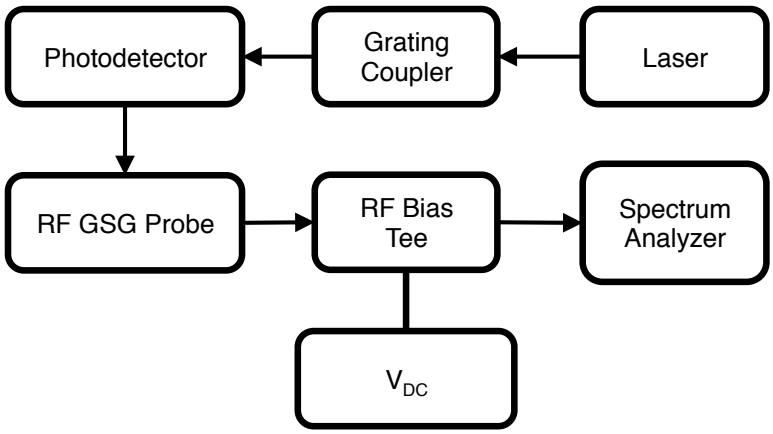

Figure 17 - Flicker noise measurement apparatus.

Flicker noise was measured using the same apparatus as for white noise. The noise power emitted by the photodetector was sampled using the RSA6114A spectrum analyzer until it asymptotically approached the white noise floor. Next, the RF GSG probe was replaced by a 50Ω terminator and the same data was taken. The difference between the noise emitted by the device and the 50Ω terminator is plotted in Fig. 16.

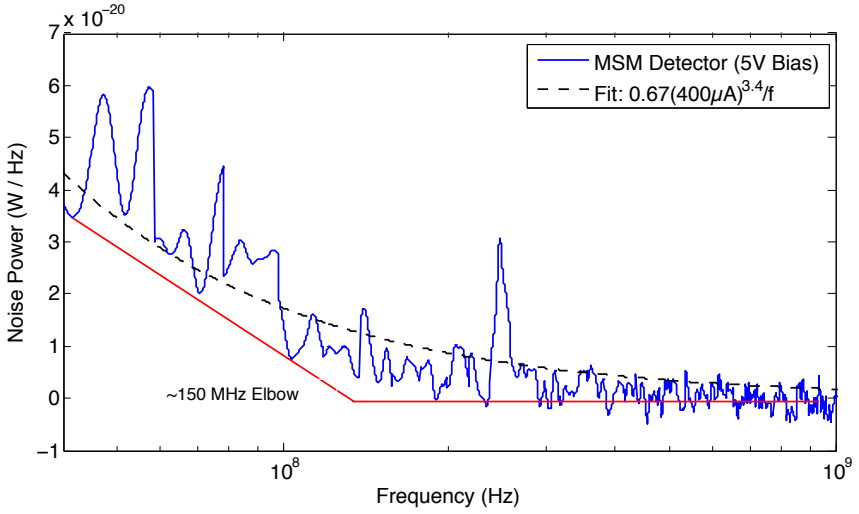

Figure 18 - Flicker noise measured data at 5 V bias and 1/f fit of measured data.

In Fig. 5, 'K_f' is 0.67, 'a' is 3.4, 'γ' is 1.0, and I_{DC} is approximately 400 μA for a 5 V contact potential for the curve fitting function associated with flicker noise.

Flicker noise is generally quantified by a metric known as the noise elbow. This is the point at which the spectrally invariant noise floor, composed of shot and thermal noise, merges with the flicker noise [11]. Once the location of the noise elbow is identified, the total noise emitted by the device can be predicted for an arbitrary frequency. The noise elbow for this device when biased at 5V is located at approximately 150 MHz, as shown in Fig. 16. At frequencies lower than 150 MHz, the sensitivity of the detector will decrease as the inverse of the frequency.

Chapter 7. Conclusions

A waveguide-coupled Si-Ge photoconductive detector with gain exceeding unity quantum efficiency and not limited by shot noise has been designed, fabricated and measured. A summary of the measured device metrics is as follows: 10.6±0.96 fF capacitance, 1.76A/W responsivity, 1.1GHz bandwidth, a 150MHz noise elbow, and a

spectrally white noise power output of at most -173.9dBm/Hz at frequencies beyond the noise elbow in a 50Ω environment. The measurements suggest that these photoconductive detectors have the attractive property that at least a significant portion of the dark current does not contribute to shot noise in the system. This means that the large dark currents seen in these detectors may not be a limitation on high-frequency performance.

In addition, theory describing critical photodetector metrics has been examined. The computational physics algorithms involved in designing the cavities through which the electromagnetic radiation propagates have been discussed. Noise mechanisms including shot and thermal noise have been derived from first principles.

References

[1] L. Vivien, M. Rouvière, J.-M. Fédéli, D. Marris-Morini, J. F. Damlencourt, J. Mangeney, P. Crozat, L. E. Melhaoui, E. Cassan, X. L. Roux, D. Pascal, and S. Laval, "High speed and high responsivity germanium photodetector integrated in a Silicon-On-Insulator microwaveguide," Opt. Express **15**, 9843-9848. (2007).

[2] M. Hochberg and T. Baehr-Jones, "Towards fabless silicon photonics," Nat. Photonics **4**, 49-494 (2010).

[3] R. Soref, "The past, present and future of silicon photonics," IEEE J. Sel. Top. Quantum Electron **12**(6), 1678–1687 (2006).

[4] L. Chen and M. Lipson, "Ultra-low capacitance and high speed germanium photodetectors on silicon," Opt. Express **17**, 7901-7906. (2009).

[5] S. Assefa, F. Xia, S. W. Bedell, Y. Zhang, T. Topuria, P. M. Rice, and Y. A. Vlasov, "CMOS-integrated high-speed MSM germanium waveguide photodetector," Opt. Express **18**, 4986-4999. (2010).

[6] C. T. DeRose, D. C. Trotter, W. A. Zortman, A. L. Starbuck, M. Fisher, M. R. Watts, and P. S. Davids, "Ultra compact 45 GHz CMOS compatible Germanium waveguide photodiode with low dark current," Opt. Express **19**, 24897-24904. (2011).

[7] L. Vivien, A. Polzer, D. Marris-Morini, J. Osmond, J. M. Hartmann, P. Crozat, E. Cassan, C. Kopp, H. Zimmermann, and J.-M. Fédéli, "Zero-bias 40Gbit/s germanium waveguide photodetector on silicon," Opt. Express **20**, 1096-1101. (2012).

[8] L. Vivien, D. Marris-Morini, J.-M. Fedeli, M. Rouviere, J.-F. Damlencourt, L. E. Melhaoui, X. L. Roux, P. Crozat, J. Mangeney, E. Cassan, and S. Laval, "Metal-semiconductor-metal Ge photodetectors integrated in silicon waveguides," Appl. Phys. Lett. **92**, 151114 (2008).

[9] S. Assefa, F. Xia and Y. A. Vlasov, "Reinventing germanium avalanche photodetector for nanophotonic on-chip optical interconnects," Nature **464**, 80-84 (2010).

[10] L. Colace, A. Scacchi, G. Assanto, "Noise characterization of Ge/Si photodetectors," in *Proc. 8th IEEE Int. Conf. Group IV Photon.*, (IEEE, 2011), pp. 290-292.

[11] B. Razavi, "Noise," in *Design of Analog CMOS Integrated Circuits*, (McGraw-Hill Companies Inc., 2001).

[12] R. Ding, T. Baehr-Jones, T. Pinguet, J. Li, N. C. Harris, M. Streshinsky, L. He, A. Novack, A. E.-J. Lim, T.-Y. Liow, S. H.-G. Teo, G.-Q. Lo, and M. Hochberg, "A high-speed silicon photonics platform," in *IEEE Photon. Conf. 2011* (IEEE, 2011), pp. 1-2.

[13] M. Levinshtein and G. S. Simin, *Getting to Know Semiconductors* (World Scientific, 1992).

[14] S. M. Sze and K. K. Ng, Physics of Semiconductor Devices, (John Wiley and Sons Inc., 2007).

[15] D. A. Neamen, *Semiconductor Physics and Devices*, (Tata McGraw-Hill Publishing Company Limited, 2007).

[16] K. M. van Vliet, "Noise Limitations in Solid State Photodetectors," Appl. Opt. **6**, 1145-1169 (1967).

[17] H. L. Hartnagel, R. Katilius, and A. Matulionis, *Microwave Noise in Semiconductor Devices*, (John Wiley and Sons Inc., 2001).

[18] W. F. Egan, *Practical RF System Design*, (John Wiley and Sons Inc., 2000).

[19] Agilent, "Fundamentals of RF and Microwave Noise Figure Measurements," http://cp.literature.agilent.com/litweb/pdf/5952-8255E.pdf.

[20] http://depts.washington.edu/uwopsis/.

[21] G. H. Golub, C. F. van Loan, *Matrix Computations*, (Johns Hopkins University Press, 1996.

[22] T. Baehr-Jones, M. Hochberg, C. Walker, E. Chan, D. Koshinz, W. Krug, A. Sherer, "Analysis of the Tuning Sensitivity of Silicon-on-Insulator Optical Ring Resonators," IEEE JLT, 23-12 (2005).